Neurobiology of Aging 45 (2016) 50–60

Contents lists available at ScienceDirect

Neurobiology of Aging

journal homepage: www.elsevier.com/locate/neuaging

# Longitudinal noninvasive magnetic resonance imaging of brain microhemorrhages in BACE inhibitor–treated APP transgenic mice

Nicolau Beckmann [a,1], Arno Doelemeyer [b,1], Stefan Zurbruegg [c], Karine Bigot [b], Diethilde Theil [b], Wilfried Frieauff [b], Carine Kolly [b], Pierre Moulin [b], Daniel Neddermann [d], Robert Kreutzer [b], Ludovic Perrot [c], Irena Brzak [c], Laura H. Jacobson [c,2], Matthias Staufenbiel [c,3], Ulf Neumann [c], Derya R. Shimshek [c,*]

[a] Musculoskeletal Diseases Department, Novartis Institutes for BioMedical Research, Basel, Switzerland
[b] Preclinical Safety Department, Novartis Institutes for BioMedical Research, Basel, Switzerland
[c] Neuroscience Department, Novartis Institutes for BioMedical Research, Basel, Switzerland
[d] Drug Metabolism and Pharmacokinetics Department, Novartis Institutes for BioMedical Research, Basel, Switzerland

ARTICLE INFO

*Article history:*
Received 8 January 2016
Received in revised form 12 April 2016
Accepted 10 May 2016
Available online 17 May 2016

*Keywords:*
Alzheimer's disease (AD)
APP23
BACE
Inhibitor
Cerebral amyloid angiopathy (CAA)
Magnetic resonance imaging (MRI)
Microbleeding
Microhemorrhage

ABSTRACT

Currently, several immunotherapies and BACE (Beta Site APP Cleaving Enzyme) inhibitor approaches are being tested in the clinic for the treatment of Alzheimer's disease. A crucial mechanism-related safety concern is the exacerbation of microhemorrhages, which are already present in the majority of Alzheimer patients. To investigate potential safety liabilities of long-term BACE inhibitor therapy, we used aged amyloid precursor protein (APP) transgenic mice (APP23), which robustly develop cerebral amyloid angiopathy. $T_2$*-weighted magnetic resonance imaging (MRI), a translational method applicable in preclinical and clinical studies, was used for the detection of microhemorrhages throughout the entire brain, with subsequent histological validation. Three-dimensional reconstruction based on in vivo MRI and serial Perls' stained sections demonstrated a one-to-one matching of the lesions thus allowing for their histopathological characterization. MRI detected small Perls' positive areas with a high spatial resolution. Our data demonstrate that volumetric assessment by noninvasive MRI is well suited to monitor cerebral microhemorrhages in vivo. Furthermore, 3 months treatment of aged APP23 with the potent BACE-inhibitor NB-360 did not exacerbate microhemorrhages in contrast to Aβ-antibody β1. These results substantiate the safe use of BACE inhibitors regarding microhemorrhages in long-term clinical studies for the treatment of Alzheimer's disease.



## 1. Introduction

Cerebral amyloid angiopathy (CAA) is a common feature of Alzheimer's disease (AD). At autopsy, approximately 80% of AD patients have been shown to display CAA (Jellinger, 2002; Vinters, 1987), characterized by extracellular amyloid-beta (Aβ) aggregate accumulation, in particular of the Aβ1-40 isoform, in the blood vessel walls of the brain (Gravina et al., 1995, Haglund et al., 2006). Furthermore, sporadic CAA (reviewed in Biffi and Greenberg, 2011; Thal et al., 2008; Vinters, 1987; Viswanathan and Greenberg, 2011; Yamada, 2000) increases with age, being rarely evident before the age of 50 years, whereas it is present in more than 50% of people older than 90 years (Vinters, 1987).

Similar to amyloid plaques, which are found at a low level in healthy elderly, mild forms of CAA often appear asymptomatic and seem to be associated with brain Aβ deposition in healthy and/or preclinical AD as well as in AD patients (Park et al., 2013; Yates et al., 2011, 2014). However, CAA may also lead to severe vascular pathologies including degeneration of smooth muscle cells and disruption of the blood-brain barrier (Itoh et al., 1993; Kawai et al., 1993; Vinters, 1987). CAA is a risk factor for cerebral hemorrhages ranging from silent microbleeds to stroke (Zhang-Nunes et al., 2006). Although about 80% of subjects with AD show CAA at

* Corresponding author at: Neuroscience Department, Novartis Institutes for BioMedical Research, Novartis Campus, 4002 Basel, Switzerland. Tel.: +41 079 543 5384.
*E-mail address:* derya.shimshek@novartis.com (D.R. Shimshek).
[1] Contributed equally.
[2] Present address: Florey Institute of Neuroscience and Mental Health and Department of Pharmacology and Therapeutics, University of Melbourne, Australia.
[3] Present address: Department of Cellular Neurology, Hertie Institute for Clinical Brain Research, University of Tübingen, Tübingen, Germany


http://dx.doi.org/10.1016/j.neurobiolaging.2016.05.009

autopsy, most of these do not suffer clinically relevant intracerebral hemorrhage (Greenberg et al., 2004). However, new reports argue that microbleeds seem to be quite common in AD and prodromal AD (Brundel et al., 2012; Kantarci et al., 2013). In vivo detection of such microhemorrhages in the human brain by imaging (reviewed by Johnson et al., 2012) gains increasing importance as these lesions potentially indicate a risk of hemorrhagic stroke or contribute to progressive cognitive dysfunction (O'Brien et al., 2003; van der Flier, 2012), although the role of CAA in the pathogenesis of AD is debated (Heringa et al., 2014; Nicoll et al., 2004; reviewed by van der Flier, 2012).

Active or passive Aβ immunotherapy has proven to be an effective means to reduce the amyloid plaque load in human or mouse brain (reviewed in Klafki et al., 2006). However, vascular Aβ transiently increased after amyloid plaque reduction during AN1792 (beta-amyloid [Aβ]1-42) immunotherapy, which suggests deposition of parenchymal Aβ in the vasculature (Boche et al., 2008). No damage of vascular smooth muscle cells but increased splitting of the vessel wall was observed in the leptomeningeal vessels of immunized subjects (Sakai et al., 2014). Treatment with bapineuzumab, an Aβ antibody, appeared to increase the risk of microhemorrhages (ARIA-H), edema (ARIA-E), and CAA (Arrighi et al., 2016; Roher et al., 2013; Salloway et al., 2009).

Different amyloid precursor protein (APP) transgenic mouse lines show a varying degree of CAA (reviewed by Klohs et al., 2014). APP23 mice develop relatively strong CAA (Calhoun et al., 1999; Kuo et al., 2001) that may be associated with microhemorrhages (Winkler et al., 2001). In some studies using APP transgenic mice passive immunization led to an increase in CAA and microhemorrhages (Beckmann et al., 2011; Luo et al., 2012; Meyer-Luehmann et al., 2011; Pfeifer et al., 2002; Racke et al., 2005; Wilcock et al., 2004). However, other investigations in APP mice showed no such effects (Asuni et al., 2006; Levites et al., 2006). Taken together, clinical data and findings from animal studies concerning Aβ immunotherapy raised an important mechanism-related safety concern possibly relevant to all Aβ-lowering treatments (Sperling et al., 2011).

It is currently unknown if beta site APP cleaving enzyme (BACE-1) (β-secretase) inhibitor treatment may lead to cerebral microhemorrhages, and an assessment of the risk in preclinical studies is therefore urgently needed. In this study, we chronically treated aged APP23 mice with the BACE inhibitor, NB-360 (Neumann et al., 2015). The β1 antibody (Paganetti et al., 1996) was used here as positive control, as previous studies revealed that treatment with the β1 antibody increased microvascular lesions in the brains of APP23 mice (Beckmann et al., 2011; Pfeifer et al., 2002). We show that 3-dimensional (3D) $T_2^*$-weighted magnetic resonance imaging (MRI) during the treatment period provided a sensitive detection of microhemorrhages, comparable with postmortem histological evaluation. Both methods did not show any signs of exacerbation of microhemorrhages in APP23 mice upon BACE inhibitor treatment. In contrast, increased microhemorrhage formation was found in the brains of APP23 mice treated with the β1 antibody.

## 2. Materials and methods

### 2.1. Ethics statement

Experiments were carried out in accordance with the guidelines of the Swiss Federal and Cantonal veterinary offices for care and use of laboratory animals. Studies described in this report were approved by the Swiss Cantonal Veterinary Authority of Basel City, Switzerland and performed according to animal license number BS-2063. Compound dosing as well as data acquisition and analyses were performed by investigators blinded to experimental treatment groups.

### 2.2. In vivo experiments: animals, compound formulation and dosing

For these studies n = 74 female APP23 transgenic mice (B6.D2-Tg (Thy1App) 23/1Sdz) and n = 20 female wild-type littermates (Novartis internal colonies, Basel, Switzerland) were used. APP23 mice express human APP751 with Swedish mutations, under the control of the murine Thy-1 promotor (Sturchler-Pierrat et al., 1997). Plaque deposition starts at approximately 6–8 months of age in APP23 mice. Female mice were used as they produce more Aβ40 and Aβ42 than males and thus show more robust and read amyloid pathology in the brain (Eisele et al., 2014; Sturchler-Pierrat and Staufenbiel, 2000).

Animals for studying spontaneous lesion development in aging APP23 mice (Fig. 1): 14 female APP23 mice were examined longitudinally by MRI from age 13.7 to 20.5 months.

BACE inhibitor NB-360/β1 antibody study (Figs. 2–5): 20 female APP23 per treatment group and 20 wild-type littermates were treated for 3 months from the age of 17.5 until 20.5 months. Animals were randomly grouped according to the number of lesions detected in the MRI before the start of the treatment. Average lesion numbers per group: $6 \pm 1$ (means ± standard error of mean [SEM]).

Mice were dosed per os chronically for 3 months with either the BACE inhibitor NB-360 (30 μmol/kg; Novartis Pharma AG, Basel, Switzerland), or vehicle. Crystalline NB-360 was formulated as a suspension. Vehicle (0.1% Tween80 in 0.5% methylcellulose in water) or compound were given in a volume of 10 mL/kg once daily (in the morning). Further animals were dosed intraperitoneally weekly for 3 months with either β1 mouse monoclonal IgG2a antibody that recognizes amino acids 3–6 of human Aβ (Paganetti et al., 1996) or mIgG control antibody (anti-Cyclosporin-A; first dose 0.4 mg/mouse, then 0.5 mg/kg).

Mice were single-housed and maintained under standard conditions in temperature and humidity controlled rooms under a 12/12 light/dark schedule, with lights on at 05:00 AM. Cage bedding consisted of sawdust and a red Perspex house (Nalgene, Thermo Fisher Scientific, Waltham, MA, USA). Nesting materials (Nestlet, Ancare, Bellmore, NY, USA) and a wooden gnawing-block were supplied in each cage. Tap water and standard laboratory rodent food were available ad libitum.

### 2.3. Magnetic resonance imaging

Three-dimensional $T_2^*$-weighted images covering the whole brain were acquired at 7 T using a Biospec 70/30 spectrometer (Bruker Medical Systems, Ettlingen, Germany) equipped with an actively shielded gradient system. The operational software of the scanner was Paravision PV5.1 (Bruker). Images were obtained using a 3D gradient-echo sequence with the following imaging parameters: repetition time 24.3 ms, echo time 10 ms, matrix $256 \times 128 \times 192$, field-of-view $1.5 \times 1.5 \times 2.4$ $cm^3$. Total acquisition time for an image having a voxel size of $59 \times 118 \times 125$ $\mu m^3$ was 10 minutes. Shimming (homogenization of the magnetic field) was performed for every animal and imaging session before acquiring a 3D image. During MRI acquisitions, mice were anaesthetized with isoflurane (Abbott, Baar, Switzerland) administered via a face mask and placed in a cradle made of Plexiglas. The head was fixed by using a tooth holder. Body temperature was maintained at $37 \pm 1$ °C via warming blankets or integrated water hoses in animal beds. Respiration and body temperature were monitored throughout the acquisition. The duration of an imaging session was about 15 minutes, including positioning of the mouse.

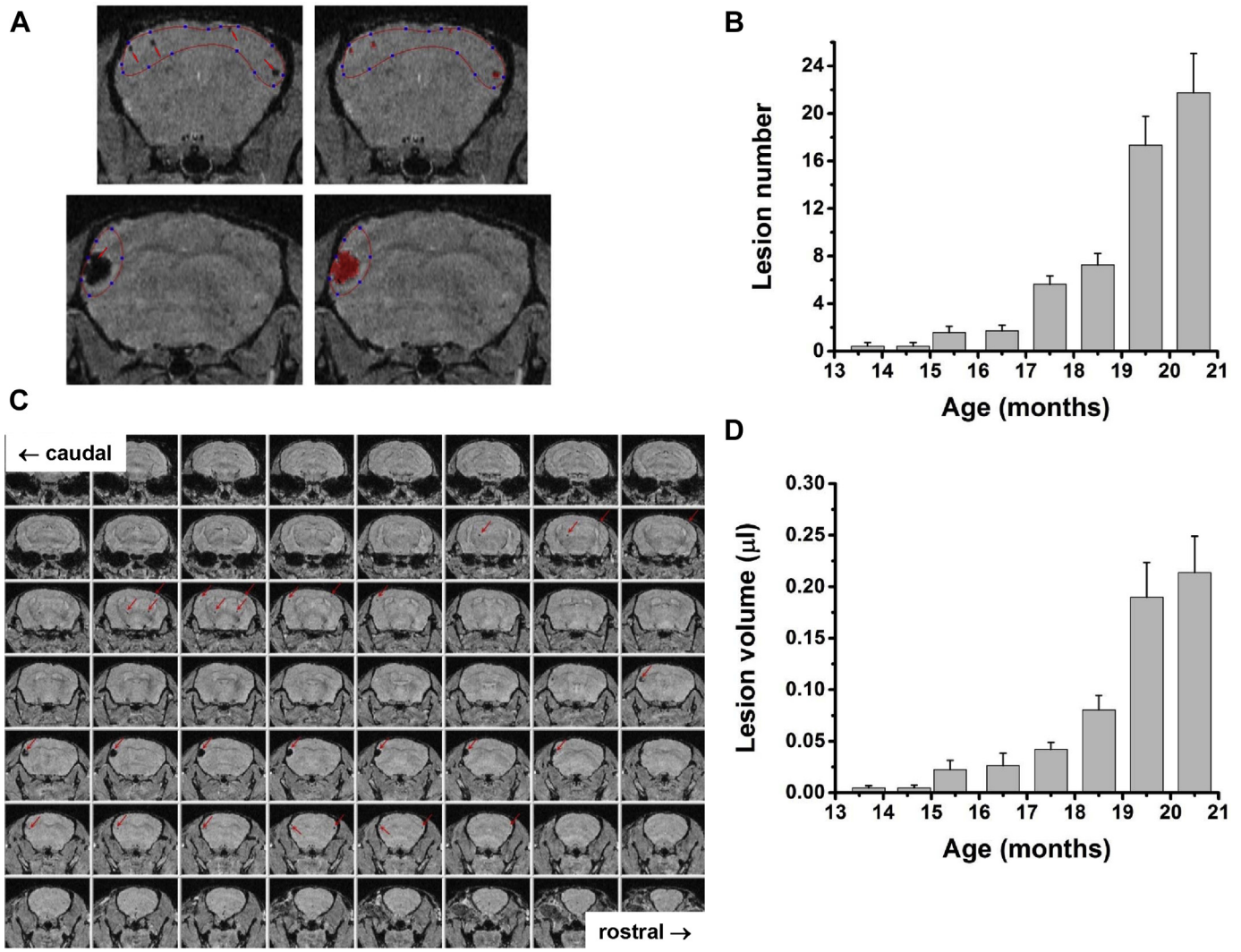


**Fig. 1.** MRI detection and distribution of brain lesions in aged APP23 mice. (A) Segmentation of lesions (red arrows) detected in the brains of APP23 mice. Two images extracted from a 3D data set are shown on the left side. On the right side, the corresponding segmented lesions are displayed. The total volume of lesions was determined by adding the segmented areas on the individual images, multiplied by the slice thickness. The red lines delimitate the regions in which lesions were segmented. (B) Number of lesions (means ± SEM, n = 14 mice at the beginning of the study) in the brains of APP23 mice, from age 13.7 to 20.5 months. (C) MR images were extracted from a 3D data and are sequentially displayed from caudal to rostral (from left to right, from top to bottom). Lesions detected by MRI (red arrows) were encountered predominantly in rostral areas of the brain. (D) Volumes of lesions shown in B (means ± SEM, n = 14 mice at the beginning of the study) in the brains of APP23 mice, from age 13.7 to 20.5 months. Abbreviations: MRI, magnetic resonance imaging; SEM, standard error of mean.

Sites in the cortex and thalamus presenting signal attenuation with a minimum diameter of 150 µm were analyzed (counts, volumes) throughout the whole brain. To ensure that the same site was not counted multiple times, its presence was carefully controlled over several consecutive slices from the 3D data set. The lesion volume was determined using specialized software (ImgTool), developed in-house. A detailed description of the software can be found in (Babin et al., 2012; Egger et al., 2013). The software has been validated and is in routine use since 2001. For each slice of the 3D data set, the areas of the signal attenuation sites within an external border were determined by applying an image segmentation algorithm. The total volume of the lesions was obtained by adding the areas assessed on the individual slices and multiplying by the slice thickness (125 µm).

Statistical analyses of lesion volumes comprised analysis of variance (ANOVA) with random effects (SYSTAT 12, Systat Software, Inc, San Jose, CA, USA) to take into account the longitudinal structure of the data. Mann–Whitney analyses (SYSTAT 12) were performed on lesion numbers. A $p < 0.05$ was considered statistically significant.

### 2.4. Postmortem analyses

At the end of the study, animals were euthanized. The brains were removed and fixed for histology, or the forebrain was frozen and used for assessments of Aβ levels.

### 2.5. Aβ measurement

#### 2.5.1. Brain homogenization

Frozen mouse forebrains were weighed and homogenized in 9 volumes (w/v) of ice-cold TBS-Complete (20 mM Tris-HCl pH 7.4, 137 mM NaCl, 1× Complete [Protease Inhibitor Cocktail Tablets: 1,836,145, Roche Diagnostics GmbH, Penzberg, Germany]) by sonication (90% duty cycle, output control 5, 40–55 pulses, [Sonifier

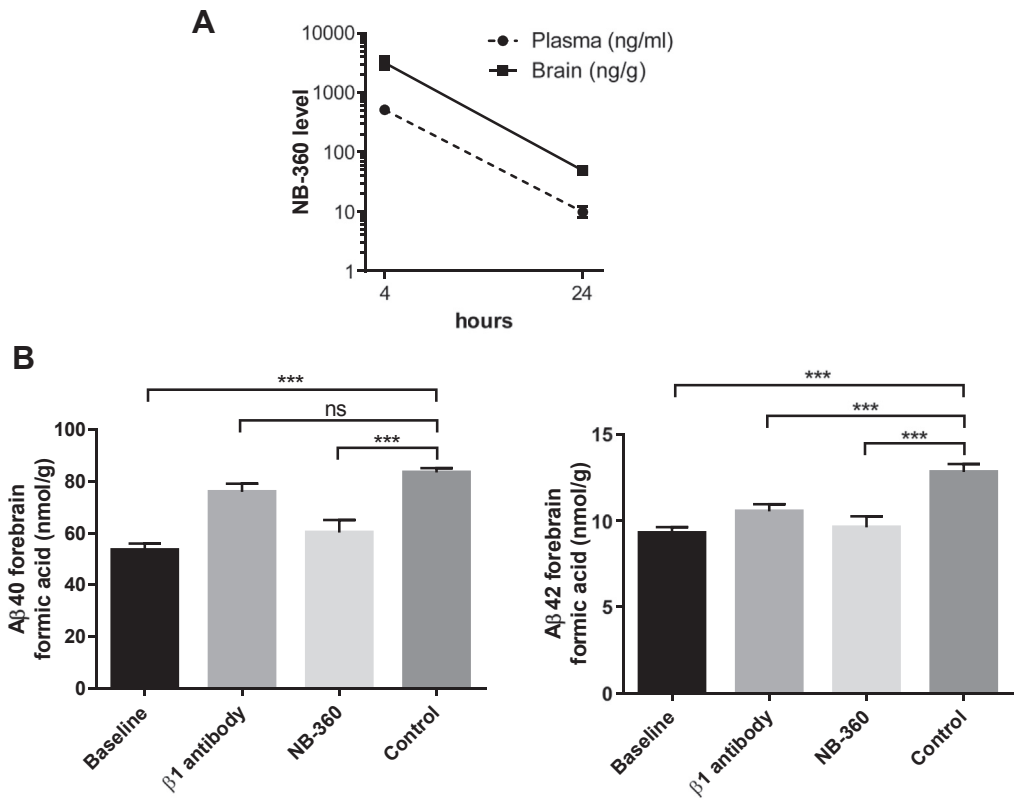


**Fig. 2.** Exposure of NB-360 in the blood and brain and pharmacodynamics effect on amyloid-β (Aβ40 and Aβ42) in the forebrain. (A) NB-360 levels in plasma and brain at 4 hour (n = 6) and 24 hour (n = 5) after last dosing (means ± SEM). (B) Aβ40 and Aβ42 determination in forebrain of treated animals at the end of the study (means ± SEM); baseline: n = 20, β1 antibody: n = 17, control: n = 15, NB-360: n = 12. The levels of significance $^{***}p < 0.001$ refer to 1-way ANOVA with Holm–Sidak's multiple comparison to the control group. Abbreviations: ANOVA, analysis of variance; MRI, magnetic resonance imaging; ns, not significant; SEM, standard error of mean.

450, Branson, Danbury, CT, USA]). After homogenization, several 50 μL aliquots were prepared for analysis and stored at −80 °C.

### 2.5.2. Extraction and determination of Aβ40 and Aβ42 in mouse forebrain

Aβ40 and Aβ42 were determined as previously described (Neumann et al., 2015) using the MSD Aβ40 and Aβ42 Ultrasensitive Kits (Meso Scale Diagnostics, Gaithersburg, MD, USA). The assays were performed according to the manufacturer's instructions and the sample preparations described as follows. TritonX-100 (TX-100) soluble Aβ was extracted from the forebrain with 1% TX-100 using a 50 μL aliquot of each 1:10 forebrain homogenate, mixed with 50 μL 2% TX-100 in TBS complete (20 mM Tris-HCl pH 7.4, 137 mM NaCl, 1× Complete [Protease Inhibitor Cocktail Tablets: 1,836,145, Roche Diagnostics GmbH, Penzberg Germany]) to reach a final concentration of 1% TX-100 and a 1:20 forebrain dilution. Samples were incubated for 15 minutes on ice and vortexed every 5 minutes. Afterward, they were centrifuged (100,000 × g, 4 °C, 15 minutes, Ultra-centrifuge) and 50 μL of the clear supernatants were transferred to fresh tubes. For the Aβ40 assay, supernatants were further diluted 1:10 in 3% Blocker A solution (from kit) to a final forebrain dilution of 1:200 and applied to the plate. Supernatants were not diluted for the determination of Aβ42. For the extraction of insoluble amyloid peptides, 50 μL forebrain homogenate was mixed with 117 μL of 100% formic acid and stored on ice for 15 minutes with vortexing. Samples were neutralized with 950 μL 1 M Tris base, containing complete protease inhibitor cocktail (Roche, Basle, Switzerland) and stored overnight at room temperature. The supernatant after 15 minutes centrifugation at 14000 rpm was used for analysis. Nontransgenic mouse forebrain homogenates spiked with synthetic Aβ were used for preparation of the standard curves and treated identically to samples. For all samples and standards, 25 μL were applied per well. The mean values from the duplicate wells were used for calculations. The relative units for samples and standards were imported into SOFTmax PRO 4.0 (Molecular Devices, Sunnyvale, CA, USA) for calculation of standard curves and quantification of samples.

## 2.6. Determination of NB-360

The determination of NB-360 in mouse plasma was performed after protein precipitation followed by liquid chromatography–mass spectrometry/mass spectrometry using electrospray ionization in positive mode. Brain samples were homogenized with 4 volume equivalent of acetonitrile and/or water (1/1), and processed like the plasma samples.

### 2.6.1. Plasma analyses

To an aliquot of 20 μL of plasma sample, 40 μL of acetonitrile containing an internal standard were added. After vortex mixing for a few seconds, samples were centrifuged for 10 minutes at 50,000 g and at 8 °C. An aliquot of 40 μL of supernatant was transferred to an autosampler vial and 40 μL of water were added, before analysis.

### 2.6.2. Brain analyses

*2.6.2.1. Homogenization.* Brain samples were weighed and homogenized with 4 volume equivalents of a mixture of acetontrile and/or water (1/1, v/v) in appropriate Lysing Matrix tubes with a homogenizer at 5000 oscillations for 30 seconds. Afterward,

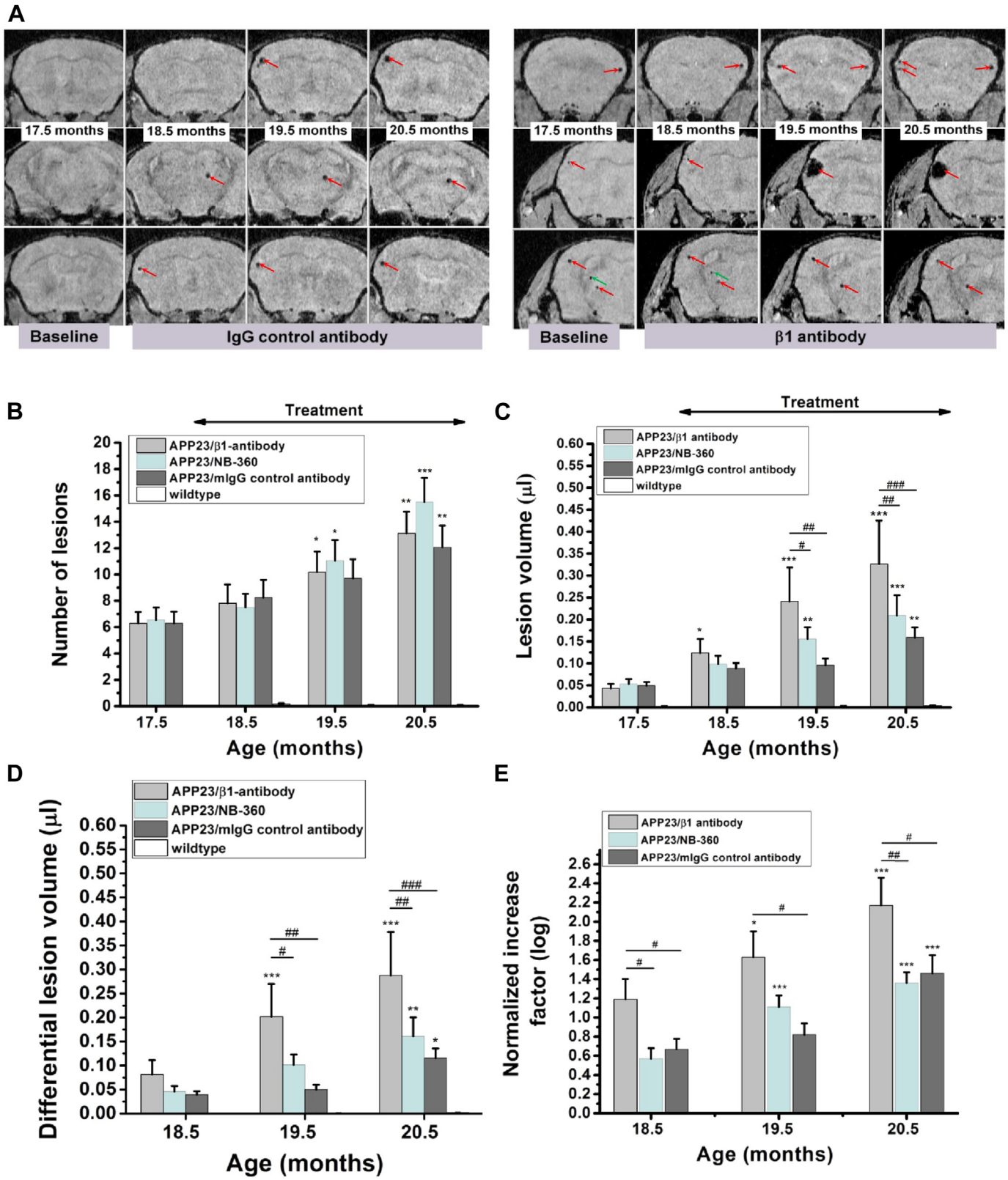


**Fig. 3.** MRI of APP23 female mice treated with either β1 antibody, BACE inhibitor NB-360, or control IgG2 antibody for 3 months. (A) MRI images of a mouse treated with the control antibody (left) and with the β1 antibody (right) from different brain areas at baseline and after 1, 2, and 3 months of treatment. Three slices at approximately the same anatomical location and extracted from 3D data sets are shown per time point. Red arrows point to a lesion that persists, green arrows point to a lesion that disappears. (B) Mean number of lesions in the whole brain (means ± SEM, n = 20 mice per group at the beginning of the study). The levels of significance $^{*}0.01 < p < 0.05$, $^{**}0.001 < p < 0.1$, and $^{***}p < 0.001$ refer to Mann–Whitney comparisons with respect to baseline values. (C) Lesion volume (means ± SEM). The levels of significance $^{*}0.01 < p < 0.05$, $^{**}0.001 < p < 0.1$, and $^{***}p < 0.001$ refer to ANOVA with random effects comparisons to baseline values, within each group. The levels of significance $^{\#}0.01 < p < 0.05$, $^{\#\#}0.001 < p < 0.1$, and $^{\#\#\#}p < 0.001$ refer to ANOVA with random effects comparisons as indicated. (D) Differential, baseline-subtracted lesion volume (means ± SEM). The levels of significance $^{*}0.01 < p < 0.05$, $^{**}0.001 < p < 0.1$, and

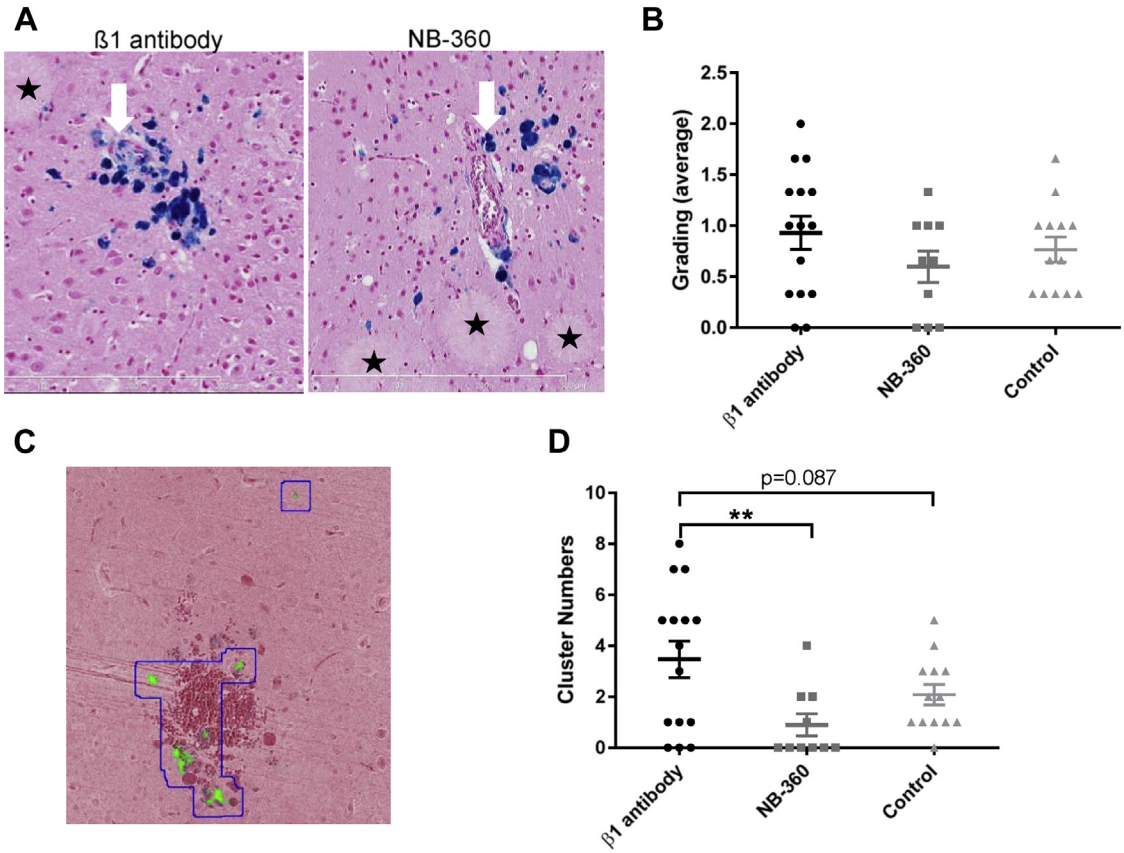


**Fig. 4.** Histopathological analyses of mice treated with either β1 antibody, BACE inhibitor NB-360 or control IgG2 antibody for 3 months. (A) Histological sections stained with Perls' Prussian blue and hematoxylin and/or eosin indicate the presence of hemosiderin (white arrow). The black asterisks depict parenchymal amyloid plaques. (B) Grading by a pathologist of the Perls' Prussian blue stained sections (n = 3 per mouse). (C) Histological section depicting clusters of Perls' Prussian blue staining obtained by ASTORIA analyses. (D) Quantification of the cluster numbers of Perls' Prussian blue stained sections (mean ± SEM). Significance levels *p* refer to 1-way ANOVA Holm-Sidak's multiple comparisons to the β1 antibody–treated group ($^{**}0.001 < p < 0.01$). β1 antibody: n = 15, NB-360: n = 10, control: n = 13. Abbreviations: ANOVA, analysis of variance; MRI, magnetic resonance imaging; SEM, standard error of mean.

homogenates were centrifuged for 10 minutes at 16,000 g, and supernatants were transferred to assay tubes.

*2.6.2.2. Preparation.* To an aliquot of 20 μL of homogenate sample, 40 μL of acetonitrile containing an internal standard were added. After vortex mixing for a few seconds, samples were centrifuged for 10 minutes at 50,000 g and at 8 °C. An aliquot of 40 μL of supernatants was transferred to an autosampler vial and 40 μL of water were added, before analysis.

### 2.7. Histology and image analysis

#### 2.7.1. Brain analyses: Perls' Prussian blue reaction for hemosiderin detection

The Perls' Prussian blue reaction was performed at 37 °C on formalin-fixed paraffin-embedded tissue sections of approximately 5 μm thickness using the Iron Staining Kit (Ventana/Roche, Tucson, AZ, USA) on the VENTANA BenchMark Special Stains automated slide stainer (Ventana/Roche). Formalin-fixed paraffin-embedded sections were deparaffinized and rehydrated followed by application of 200 μL Iron Reagent A (Ventana/Roche) for 4 minutes and subsequent application of 200 μL Iron Reagent B (Ventana/Roche) for another 4 minutes. Finally, 200 μL Iron NuclearFast Red (NFR; Ventana/Roche) was applied on each slide. After counterstaining with NFR (Ventana/Roche), the slides were dehydrated and mounted using Pertex (Biosystems Switzerland, Nunningen, Switzerland).

The distribution, size, and staining intensity of hemosiderin depositions were assessed by light microscopy with a special focus on their association with blood vessel and Aβ plaques brain sections located at the level of optic chiasm, anterior midbrain, and posterior colliculus. The grading criteria for hemosiderin deposition in the brain were based on the following scale for reporting pathological changes (Zago et al., 2013): minimal (grade 1), very small hemosiderin deposits ± association with blood vessels and/or beta-amyloid plaque; mild (grade 2), small hemosiderin foci associated with blood vessels and/or beta-amyloid plaques; moderate (grade 3), moderate-sized hemosiderin foci associated with blood vessels and/or plaques.

$^{***}p < 0.001$ refer to ANOVA with random effects comparisons to baseline values, within each group. The levels of significance $^{\#}0.01 < p < 0.05$, $^{\#\#}0.001 < p < 0.1$, and $^{\#\#\#}p < 0.001$ refer to ANOVA with random effects comparisons as indicated. (E) Corresponding normalized lesion volume increase factor detected by MRI in the whole brain (mean ± SEM). The levels of significance $^{*}0.01 < p < 0.05$ and $^{***}p < 0.001$ refer to ANOVA with random effects comparisons to factors determined at 18.5 months of age, within each group. The levels of significance $^{\#}0.01 < p < 0.05$ and $^{\#\#}0.001 < p < 0.01$ refer to ANOVA with random effects analyses as indicated. Abbreviations: ANOVA, analysis of variance; MRI, magnetic resonance imaging; SEM, standard error of mean.

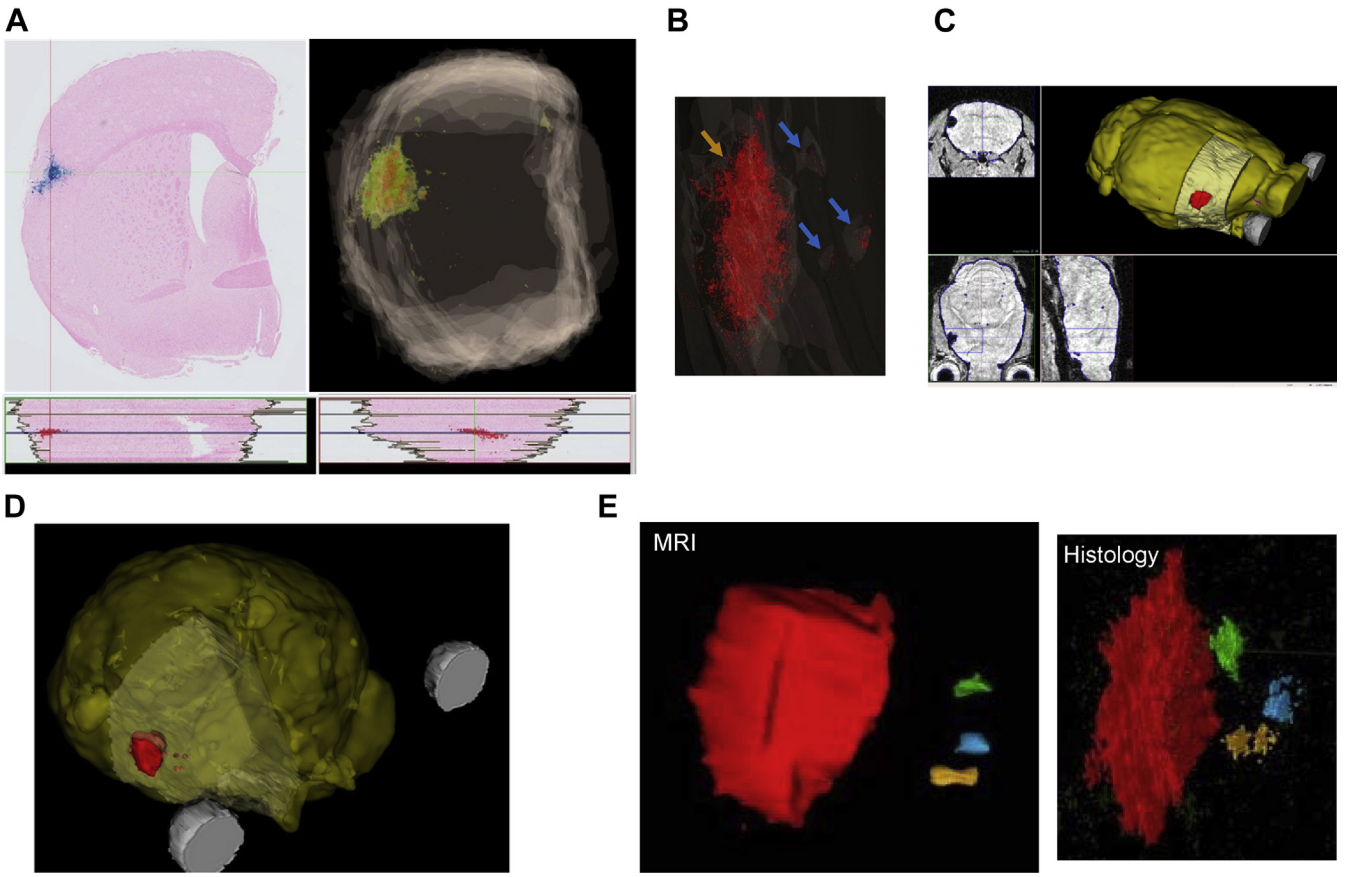


**Fig. 5.** Three-dimensional reconstruction of MRI and histological sections. (A) Serial Perls' Prussian blue stained sections were aligned, rotated, and shifted for 3D reconstruction. (B) Lesion visualized by Perls' Prussian blue was detected, and a hull around the detected segments was constructed. Orange arrow: major lesion; blue arrows: minor lesions. (C) Three-dimensional reconstruction of the MRI images. Pale yellow depicts the area covered by the histological sections, red the Perls' Prussian blue staining. (D) Three-dimensional reconstruction of the MRI images as in (C), but the brain area was rendered transparent to visualize the lesions inside it shown in light red, whereas the portion of lesion on the brain surface is marked in dark red. (E) Rendering of reconstructed lesions for MRI (left) and histology (right). Abbreviations: MRI, magnetic resonance imaging; SEM, standard error of mean.

Statistical analyses of the grading of lesions comprised 1-way ANOVA with Dunn's multiple comparison tests (GraphPad Prism V6.04, GraphPad Software, Inc, La Jolla, CA, USA).

### 2.7.2. Image analysis

For the quantitative microhemorrhage evaluation based on image analysis, a proprietary image analysis platform (ASTORIA, Automated Stored Image Analysis) was developed in-house (Novartis Preclinical Safety, Basel, Switzerland) based on MS Visual Studio 2010 and many functions from Matrox MIL V9 libraries (Matrox Inc, Quebec, Canada).

For the hemosiderin deposit analysis, the following sequence of steps was performed: (1) Slide scanning with a Hamamatsu Nanozoomer (20×; Hamamatsu Photonics, Solothurn, Switzerland); (2) automated detection of brain sections (Fast Red staining) on the scans to generate region of interest and creation and export of tif image tiles within the region of interest using the proprietary ImageScope (Aperio Inc, Vista, CA, USA) plug-in; and (3) image batch processing with the ASTORIA image analysis platform for detection of a valid brain area (Fast Red staining), various thresholding techniques and morphological transformations for segmentation of bluish (Perls' positive) objects, rejection of objects too close to the brain section's periphery to exclude bleeding due to mechanic rupture of tissue, rejection of staining artifacts, feature based object classification, and determination of clusters.

The image analysis for hemosiderin deposit detection and measurement comprised the following steps: (1) extract red, green, and blue channels from stored tif images as gray images; (2) get a valid sample area through adding difference red-green channel to difference red-blue channel image, binarization by thresholding. Add sufficiently high signal in blue-red difference to include heavily blue stained objects; (3) perform morphological closing, opening, and filling of holes (Matrox Imaging Library, Rauscher, Olching, Germany); (4) remove sample edges from a valid range by subtracting dilated background; (5) segment bluish hemosiderin deposits by starting from blue:red ratio and thresholding to obtain "maximum" markers, then reconstruct from "minimal" markers (seeds) that fulfilled a minimum blue:red ratio requirement (Matrox Imaging Library); (6) add objects from thresholded HSI (Hue, Saturation, Intensity) image; (7) restrict the maximum intensity in the red channel to exclude heavily pink-stained objects; (8) get minimal seed markers through binarization on the blue-red image and size filtering; then reconstruct to obtain sets of all valid objects. Restrict to a valid sample range (see [3] previously mentioned); (9) determine and remove too bright regions (based on HSI); (10) remove objects that did not extend sufficiently far from the image frame; (11) individually classify objects based on morphometric and densitometric features: an "artifact" class was characterized by morphometric object features (size, shape) or amount of "darkness" in the blue channel, i.e. too dark (black dust) features. Objects falling in this class were disregarded from the

analysis. Various combinations of gray features in the red, green, and blue channels with morphometric features (size, shape) were used to determine valid hemosiderin deposits and to exclude artifacts. Each of these filter criteria had to be determined for a valid object; (12) define clusters by 100 dilations and 70 erosions of the detected objects (generate large images by including neighbor tiles). A valid cluster consisted of at least 2 valid objects that had passed step (10); and (13) store morphometric and densitometric features for each hemosiderin object for statistical analysis.

The parameters measured for each sample were (1) Perls' positive ratio (total blue area vs. total brain section area), (2) number of individual hemosiderin deposits (blue objects), and (3) number of clusters ($\geq$2 deposits within limited distance). Assessment using the average of 3 sections for each animal was considered to be representative and in line with the pathologist's assessment for grading.

Statistical analyses comprised 1-way ANOVA with Holm–Sidak's multiple comparison tests (GraphPad Prism V6.04).

### 2.8. Three-dimensional reconstruction from histological serial sections and MRI images

Three-dimensional reconstructions were performed from serial histological sections and coregisteration of the reconstructed volume to the MRI data using a stereotactic Allen mouse brain atlas (http://mouse.brain-map.org/static/atlas, Allen Institute for Brain Science, Seattle, WA, USA) for positional reference. Image analysis was conducted on the Perls' stained histological sections and the MRI data with Definiens Developer XD software (Developer XD 2.0, Definiens, Munich, Germany), using specifically developed image analysis algorithms.

#### 2.8.1. Histology sample preparation

The anterior part of half a brain was cut into serial coronal sections of approximately 5 μm thickness, using a microtome with a cool cut head. The region taken corresponded to stereotactic coordinates in the mouse brain atlas (Franklin and Paxinos, 2008) plates 15–40 (approximately interaural position 5.74–3.74). Two consecutive sections were placed on each glass slide. Assessment of hemosiderin deposition was performed by the Perls' Prussian blue reaction as described above.

#### 2.8.2. Digital whole-slide scanning

Glass slides were scanned for subsequent image analysis using a Philips slide scanner (Philips Ultra-Fast Scanner, version 1.6 & Image Management System, version 2.2, Philips Digital Pathology, Best, The Netherlands). A 40× objective was used for scanning, resulting in a pixel size of 0.25 μm in x and y directions.

#### 2.8.3. Three-dimensional reconstruction from serial histological sections

Tissue sections were detected in the digital slide scans and aligned using linear affine transformation, matching the center of gravity and the direction of the main axis. Sections lost (37 lost sections [8%] due to technical issues) in the preparation process were replaced by repeating previous sections. Perls' staining was detected using color deconvolution and subsequent thresholding.

#### 2.8.4. Three-dimensional reconstruction from MRI data

MRI data were exported into tif file format, resampling the non-uniform x and y image matrix (pixel size x: 59 μm; y: 117 μm) to result in a square image matrix. The resampled images were then analyzed using a specifically designed algorithm to delineate the area of the brain and the areas of signal attenuation representing microhemorrhages. Three-dimensional rendering of the borders of detected areas was then performed.

#### 2.8.5. Coregistration of MRI and 3D reconstructed histology data

To coregister the MRI volume and the volume sampled from histological serial sections, both data sets have been registered manually to the Allen stereotactic mouse brain atlas, identifying morphological brain features in the MRI and histological data and finding the closest corresponding z location in the atlas. Thus, the atlas coordinate system has been established as the common coordinate system for both data sets. To aid the visualization of the coregistered data set, the MRI data have been resampled to approximately match the pixel resolution imposed by the histological sections. Frame interpolation software (slowmoVideo, http://slowmovideo.granjow.net/, Simon A. Eugster, bachelor thesis ETH Zurich, Zurich, Switzerland) has been used to add frames to the MRI data to change the z-slice distance from 125 μm to approximately 5 μm. Bicubic interpolation has been used for x and y coordinates to match the resolution of the digital slide scan data of the histological slides.

## 3. Results

### 3.1. Quantification of microhemorrhages in aged APP23 mice using $T_2^*$-weighted MRI

Aged APP23 animals display microhemorrhages in different parts of the brain (Winkler et al., 2001). These events can be visualized by $T_2^*$-weighted MRI as sites of attenuated signals (Fig. 1A) and their number quantified (Beckmann et al., 2011). In agreement, MRI-detectable microhemorrhages in the present study started to appear at the age between 15 and 17 months and gradually increased in number (Fig. 1B). Most of the lesions were detected in the rostral part of the brain and appeared isolated and randomly distributed (Fig. 1C, red arrows). The caudal part was devoid of lesions at ages up to 20.5 months in APP23 mice (Fig. 1C). To obtain a better measure of their severity, we determined the total lesion volume per mouse brain. A substantial increase was detected during the aging process with an average lesion volume of 0.04 ± 0.07 μL (means ± SEM, n = 14 mice) at 17.5 and 0.21 ± 0.04 μL (means ± SEM, n = 12 mice) at 20.5 months of age (Fig. 1D). As expected from histological analyses of microhemorrhage (Winkler et al., 2001), the total lesion volume determined for each mouse brain varied considerably. It ranged from 0.01 to 0.13 μL at 17.5 months of age and from 0.13 to 0.42 μL at 20.5 months of age. Taken together aged APP23 displayed sparse and random microhemorrhages in cortical and thalamic areas of the rostral brain. The number and volume of these lesions could be quantified using $T_2^*$-weighted MRI which demonstrated an increase with age.

### 3.2. BACE inhibitor treatment did not aggravate microhemorrhage in aged APP23 mice

We next treated aged APP23 animals for 3 months (from 17.5 to 20.5 months of age) with the very potent and brain-penetrable BACE inhibitor NB-360 at a high therapeutic dose of 30 μmol/kg/day (Neumann et al., 2015). As a positive control, we used the β1 antibody (Paganetti et al., 1996) which is known to induce microhemorrhages in APP23 (Pfeifer et al., 2002). Plasma and brain

exposures of NB-360 were similar to earlier studies (Fig. 2A [Neumann et al., 2015]). Body weight of APP23 animals was reduced by approximately 25% compared to wild-type mice but did not differ between the different treatment groups (data not shown). NB-360 treatment of aged APP23 resulted in a significant lowering of Aβ40 and Aβ42 in the forebrain compared with vehicle treatment (Fig. 2B). No significant difference from baseline was found after a 3-month BACE inhibitor treatment (Fig. 2B). Mice immunized with the β1 antibody showed a significant reduction of Aβ42 but not Aβ40 in the forebrain (Fig. 2B) as described earlier (Pfeifer et al., 2002). Thus, BACE-inhibitor treatment and passive immunization were highly effective in lowering forebrain Aβ in aged APP23 mice.

Longitudinal $T_2^*$-weighted MRI measurements (Fig. 3A) of vehicle-treated animals (nonrelevant antibody) showed an age-dependent increase in lesion number and volume (Fig. 3B and C). Changes of both parameters in NB-360 treated mice were similar and not significantly different from the vehicle-treated APP23 (Fig. 3B and C). In contrast, a significantly greater increase in lesion volume (absolute and differential, baseline-subtracted volume) but not lesion number was found in β1 immunized compared with vehicle-treated animals (Fig. 3B–D). In a few of β1 immunized mice very large lesions (>1 μL) were detected, which were absent in the other treatment groups (Fig. 3A). Furthermore, the relative lesion volume increase for each individual animal, i.e. the total lesion volume at study end divided by the corresponding volume at baseline was calculated and resulted in similar changes (Fig. 3E). One animal in the β1 group that had no lesion at the start of the study was excluded from this analysis. In summary, BACE-inhibitor treatment for 3 months did not aggravate MRI-assessed microhemorrhage development in aged APP23 mice in contrast to the β1 antibody serving as positive control.

After 3 months of treatment, APP23 animals were killed and their brains subjected to histological analyses. Perls' staining was performed on 3 different brain sections, and hemosiderin deposits were graded (see Material and Methods) by a pathologist blinded to treatment groups (Fig. 4A and B). Hemosiderin staining was observed in the APP23 mice irrespective of the treatment group. Only minimal-to-mild hemosiderin deposition was found in BACE-inhibitor NB-360 treated (39% of animals) and vehicle-treated (27% of animals) mice. In contrast, mild-to-moderate hemosiderin deposition was detected after β1 treatment (44% of animals). Thus, BACE-inhibitor NB-360 did not increase the severity of the hemosiderin deposits (Fig. 4B). In β1-antibody immunized APP23 mice only a slight, nonsignificant increase in the severity of hemosiderin deposition was observed (Fig. 4B). Concerning the appearance and distribution of the hemosiderin deposits no differences were noted between NB-360, β1-antibody, and vehicle-treated animals.

A more refined quantification of microhemorrhages was performed by image analysis using ASTORIA (Fig. 4C and D). The stained sections were scanned and analyzed for Perls' stained area (stained area normalized to the total area), deposits (individual hemosiderin deposits [blue objects]), and clusters (≥2 deposits within limited distance). The Perls' stained area (means ± SEM, $\times 10^7$) was similar in NB-360 ($98.5 \pm 40.9$, $n = 10$) and vehicle-($101.5 \pm 21.2$, $n = 13$) treated mice. The β1 group ($255.9 \pm 127.4$, $n = 15$) was greater than the vehicle group, but the difference was not statistically significant ($p = 0.382$, NB-360 vs. β1-antibody group, 1-way ANOVA Holm–Sidak's multiple comparison test). Similarly, the numbers of Perls' positive deposits (means ± SEM) were comparable for the NB-360 ($4.2 \pm 0.7$, $n = 10$) and vehicle ($7.2 \pm 1.5$, $n = 15$) group and higher in the β1-antibody group ($8.6 \pm 1.9$, $n = 15$) but without reaching statistical significance ($p = 0.139$, NB-360, 1-way ANOVA Holm–Sidak's multiple comparison test). Finally, cluster analysis (Fig. 4C) revealed lower cluster numbers in BACE-inhibitor NB-360 and vehicle-treated APP23 mice compared with mice immunized with the β1 antibody (Fig. 4D). Taken together, the quantitative assessment of hemosiderin deposition using digital image analysis on only a limited number of brain sections confirmed the MRI-assessed increase in microhemorrhages after β1 immunotherapy but not NB-360 treatment. Furthermore, Perls' positive clusters and deposits correlated significantly with the MRI lesion volume (Pearson $r = +0.549$, $p < 0.0004$, and $r = +0.463$, $p < 0.0039$, respectively) but not with the MRI lesion numbers (Pearson $r = +252$, $p = 0.132$ and $r = +0.271$, $p = 0.105$, respectively).

### 3.3. Three-dimensional reconstruction from histological serial sections and MRI images reveals sufficient sensitivity of in vivo volumetric microhemorrhage assessment by MRI

To evaluate the sensitivity of $T_2^*$-weighted MRI measurements in detecting microhemorrhages in the APP23 mouse brain, we compared MRI and histological sections from one animal. First, a 3D reconstruction of histological sections needed to be established. For this, sequential coronal sections (468 sections) from the anterior part of a brain half were collected, then stained with Perls' and scanned. For an aligned stack of images, the scanned serial sections were rotated and shifted. Finally, microhemorrhages, which are Perls' positive, were assessed by image analyses, and a hull was added around detected segments (Fig. 5A). In this stack of images of this animal 4 hemosiderin clusters could be observed (Fig. 5B). Besides the very big microhemorrhage (Fig. 5B, brown arrow), 3 smaller hemosiderin positive clusters were visible (Fig. 5B, blue arrows).

To compare the stack of histological sections to the $T_2^*$-weighted MRI measurements, MRI images (125 μm slice distance) from the same animal were 3D reconstructed (Fig. 5C, dark yellow). The brain area for which sections were histologically processed is marked in light yellow color (Fig. 5C), and the large lesion detected by MRI is shown in red (Fig. 5C). This big lesion was located on the surface of the brain, whereas the other smaller lesions were found inside the brain, which can be visualized by rendering the brain transparent (Fig. 5D). Similar to histology, 4 lesions in this brain area could be detected by $T_2^*$-weighted MRI. To demonstrate that lesions detected by Perls'staining and MRI were identical, MRI in vivo imaging and histological sections were combined by co-egistration and rendering both data sets. The rendering of the reconstructed lesions are shown in Fig. 5E, for $T_2^*$-weighted MRI and histology with the same color code. The corresponding lesions, shown with different colors, reveal a one-to-one match of lesions of Perls' stained-sections and in vivo $T_2^*$-weighted MRI measurements (Fig. 5E). Thus, MRI and histopathology correlated very well and MRI detected small Perls' positive clusters with sufficient extent along the z-axis. Taken together, volumetric assessment by $T_2^*$-weighted MRI is very sensitive and detects small lesions with a high spatial resolution and thus supports in vivo monitoring of cerebral microhemorrhages in animal studies.

## 4. Discussion

Immunotherapies against Aβ have shown an increased incidence of microhemorrhages (Arrighi et al., 2016; Bayer et al., 2005; Gilman et al., 2005; Orgogozo et al., 2003; Roher et al., 2013; Salloway et al., 2009). This raises more general safety concerns regarding all therapeutic approaches directed against Aβ including the extensively studied β-secretase (BACE1) inhibition. We used an APP-transgenic mouse model to test chronic BACE-inhibitor NB-360 treatment for effects on microhemorrhages. For these studies, APP23 mice have been chosen as animal model because they develop extensive CAA and microhemorrhages during aging (Winkler et al., 2001). MRI during the treatment followed by

postmortem histological confirmation did not reveal an increase in microhemorrhages by BACE inhibition in contrast to Aβ immunotherapy tested in parallel. $T_2$*-weighted MRI revealed an age-dependent increase of lesion volume in the control group. Furthermore, a more profound enhancement of MRI lesion volume after β1-antibody treatment was obvious. A 6.5-fold increase of the lesion volume quantified by MRI in vivo could be observed in APP23 females treated with the β1 antibody compared with a 3-fold increase in the control group, the latter showing the aging effect in the APP23 mice. Lesion numbers measured by $T_2$*-weighted MRI increased also during aging as reported previously (Beckmann et al., 2011). However, we did not observe an increase of $T_2$*-weighted MRI lesion numbers in the β1-treatment group compared with control mice. The sensitivity of MRI in combination with the intravenous administration of iron oxide nanoparticles (superparamagnetic iron oxide [SPIO]) to noninvasively monitor the development of vascular pathology and its possible enhancement by Aβ immunotherapy in transgenic mice modeling AD has been shown earlier (Beckmann et al., 2011). Consistent with the ability of SPIO nanoparticles to label macrophages (Beckmann et al., 2009), histology of sites displaying signal attenuation in the MRI brain images demonstrated the presence of iron-containing macrophages in the vicinity of CAA-affected blood vessels (Beckmann et al., 2011). In that work, treatment with the β1 antibody after a similar protocol as adopted here (including the age of the animals), led to an increase of sites displaying signal attenuation in the brains of APP23 mice. This result suggests an increase in sensitivity for detecting vascular abnormalities by SPIO administration, as both the presence of iron-loaded macrophages and microhemorrhages might have contributed to the signal attenuation sites, in contrast to the present study, in which only microhemorrhages were detected by MRI.

Histopathological analyses of microhemorrhages in the brain with Perls' Prussian blue staining after 3 months treatment revealed several weak microbleeds. In standard histopathological evaluations, 3 brain sections from different parts of the brain were analyzed by blinded grading by a pathologist. Grading of the microbleeds revealed no significant differences between the treatment groups, only a weak trend could be observed. It was noted that most of the MRI-detected lesions were concentrated in the anterior part of the brain, in the cortex, and thalamus, and no lesions were detected in the posterior part. Thus, MRI may help to direct the focus of ex vivo histopathological analyses to the respective area which will result in much more refined, robust, and representative outcomes in standard histopathological evaluations. Digital image quantification refined the histopathological analyses by counting Perls' positive staining. This quantitative image analysis showed that hemosiderin cluster analysis could offer an important advantage to reveal microhemorrhage events in the brain. By this method, we could observe a slight but not statistically significant increase of Perls' positive cluster numbers in β1-antibody treated animals compared with controls, furthermore confirming the only subtle and sparse appearance of microhemorrhages and the strong advantage of longitudinal and noninvasive MRI. This is even further substantiated when combining histological and MRI images. Three-dimensionsal reconstruction and rendering of lesions revealed that MRI detects small Perls' positive areas with sufficient extent along the z-axis that may be missed in the histological analysis of a few sections.

How microhemorrhages are induced by antibodies is still under debate; induction of inflammatory responses (Eng et al., 2004; Ferrer et al., 2004; Nicoll et al., 2003), remodelling of the vasculature after fast removal of amyloid deposits from the parenchyma, and further transient excessive Aβ deposition in the vasculature (Boche et al., 2008) have been shown to be important factors. Nevertheless, in contrast to the β1 antibody, BACE-inhibitor NB-360 treatment did not further increase any CAA-related microhemmorhages. In the present study, we used NB-360 at a dose of 30 μmol/kg/d that ensured a substantial reduction of Aβ in the brain. At this dose, brain Aβ40 and Aβ42 were significantly reduced by 28% and 25%, respectively, compared with vehicle, but not below baseline. In agreement to previous data, β1 treatment significantly reduced Aβ42 by 18% but not Aβ40 in the brain (Pfeifer et al., 2002).

Taken together, volumetric assessment by MRI enables in vivo monitoring of cerebral microhemorrhages in animal studies and reduced and refined the labor intensive work of histopathological characterization with better outcome. An additional advantage of the technique is its translational character, which is particularly relevant in the context of drug development. Furthermore, this study showed that BACE-inhibitor treatment did not increase the number or severity of microhemorrhage events.

## Disclosure statement

During the planning and execution of the experiments all authors were employees of Novartis Pharma AG, Basel, Switzerland. The study has been performed with internal funding of Novartis Pharma AG.

## References


Arrighi, H.M., Barakos, J., Barkhof, F., Tampieri, D., Jack, C., Melançon, D., Morris, K., Ketter, N., Liu, E., Brashear, H.R., 2016. Amyloid-related imaging abnormalities-haemosiderin (ARIA-H) in patients with Alzheimer's disease treated with bapineuzumab: a historical, prospective secondary analysis. J. Neurol. Neurosurg. Psychiatry 87, 106–112.

Asuni, A.A., Boutajangout, A., Scholtzova, H., Knudsen, E., Li, Y.S., Quartermain, D., Frangione, B., Wisniewski, T., Sigurdsson, E.M., 2006. Vaccination of Alzheimer's model mice with Abeta derivative in alum adjuvant reduces Abeta burden without microhemorrhages. Eur. J. Neurosci. 24, 2530–2542.

Babin, A.L., Cannet, C., Gérard, C., Saint-Mezard, P., Page, C.P., Sparrer, H., Matsuguchi, T., Beckmann, N., 2012. Bleomycin-induced lung injury in mice investigated by MRI: model assessment for target analysis. Magn. Reson. Med. 67, 499–509.

Bayer, A.J., Bullock, R., Jones, R.W., Wilkinson, D., Paterson, K.R., Jenkins, L., Millais, S.B., Donoghue, S., 2005. Evaluation of the safety and immunogenicity of synthetic Abeta42 (AN1792) in patients with AD. Neurology 64, 94–101.

Beckmann, N., Cannet, C., Babin, A.L., Zurbruegg, S., Kneuer, R., Dousset, V., 2009. In vivo visualization of macrophage infiltration and activity in inflammation using magnetic resonance imaging. Wiley Interdiscip. Rev. Nanomed. Nanobiotechnol. 1, 272–298.

Beckmann, N., Gérard, C., Abramowski, D., Cannet, C., Staufenbiel, M., 2011. Noninvasive magnetic resonance imaging detection of cerebral amyloid angiopathy-related microvascular alterations using superparamagnetic iron oxide particles in APP transgenic mouse models of Alzheimer's disease: application to passive Abeta immunotherap. J. Neurosci. 31, 1023–1031.

Biffi, A., Greenberg, S.M., 2011. Cerebral amyloid angiopathy: a systematic review. J. Clin. Neurol. 7, 1–9.

Boche, D., Zotova, E., Weller, R.O., Love, S., Neal, J.W., Pickering, R.M., Wilkinson, D., Holmes, C., Nicoll, J.A.R., 2008. Consequence of Abeta immunization on the vasculature of human Alzheimer's disease brain. Brain 131, 3299–3310.

Brundel, M., Heringaa, S.M., De Bressef, J., Koekc, H.L., Zwanenburgb, J.J.M., Kappellea, L.J., Luijtend, P.R., Biessels, G.J., 2012. High Prevalence of Cerebral Micro bleeds at 7Tesla MRI in Patients with Early Alzheimer's Disease. J. Alzheimers Dis. 31, 259–263.

Calhoun, M.E., Burgermeister, P., Phinney, A.L., Stalder, M., Tolnay, M., Wiederhold, K.H., Abramowski, D., Sturchler-Pierrat, C., Sommer, B., Staufenbiel, M., Jucker, M., 1999. Neuronal overexpression of mutant amyloid precursor protein results in prominent deposition of cerebrovascular amyloid. Proc. Natl. Acad. Sci. U S A. 96, 14088–14093.

Egger, C., Cannet, C., Gérard, C., Jarman, E., Jarai, G., Feige, A., Suply, T., Micard, A., Dunbar, A., Tigani, B., Beckmann, N., 2013. Administration of bleomycin via the oropharyngeal aspiration route leads to sustained lung fibrosis in mice and rats as quantified by UTE-MRI and histology. PLoS One 8, e63432.

Eisele, Y.S., Fritschi, S.K., Hamaguchi, T., Obermüller, U., Füger, P., Skodras, A., Schäfer, C., Odenthal, J., Heikenwalder, M., Staufenbiel, M., Jucker, M., 2014. Multiple factors contribute to the peripheral induction of cerebral β-amyloidosis. J. Neurosci. 34, 10264–10273.

Eng, J., Frosch, M., Choi, K., 2004. Clinical manifestations of cerebral amyloid angiopathy–related inflammation. Ann. Neurol. 55, 250–256.

Ferrer, I., Boada Rovira, M., Sánchez Guerra, M.L., Rey, M.J., Costa-Jussá, F., 2004. Neuropathology and pathogenesis of encephalitis following amyloid-beta immunization in Alzheimer's disease. Brain Pathol. 14, 11–20.

Franklin, K.G., Paxinos, G., 2008. The Mouse Brain in Stereotaxic Coordinates, 3rd edition. Academic Press, San Diego.
Gilman, S., Koller, M., Black, R.S., Jenkins, L., Griffith, S.G., Fox, N.C., Eisner, L., Kirby, L., Rovira, M.B., Forette, F., Orgogozo, J.-M., 2005. Clinical effects of Abeta immunization (AN1792) in patients with AD in an interrupted trial. Neurology 64, 1553–1562.
Gravina, S.A., Ho, L., Eckman, C.B., Long, K.E., Otvos Jr., L., Younkin, L.H., Suzuki, N., Younkin, S.G., 1995. Amyloid beta protein (A beta) in Alzheimer's disease brain. Biochemical and immunocytochemical analysis with antibodies specific for forms ending at A beta 40 or A beta 42(43). J. Biol. Chem. 270, 7013–7016.
Greenberg, S.M., Eng, J.A., Ning, M., Smith, E.E., Rosand, J., 2004. Hemorrhage burden predicts recurrent intracerebral hemorrhage after lobar hemorrhage. Stroke 35, 1415–1420.
Haglund, M., Kalaria, R., Slade, J.Y., Englund, E., 2006. Differential deposition of amyloid beta peptides in cerebral amyloid angiopathy associated with Alzheimer's disease and vascular dementia. Acta Neuropathol. 111, 430–435.
Heringa, S.M., Reijmer, Y.D., Leemans, A., Koek, H.L., Kappelle, L.J., Biessels, G.J., 2014. Multiple microbleeds are related to cerebral network disruptions in patients with early Alzheimer's disease. J. Alzheimers Dis. 38, 211–221.
Itoh, Y., Yamada, M., Hayakawa, M., Otomo, E., Miyatake, T., 1993. Cerebral amyloid angiopathy: a significant cause of cerebellar as well as lobar cerebral hemorrhage in the elderly. J. Neurol. Sci. 116, 135–141.
Jellinger, K.A., 2002. Alzheimer disease and cerebrovascular pathology: an update. J. Neural Transm. 109, 813–836.
Johnson, K.A., Fox, N.C., Sperling, R.A., Klunk, W.E., 2012. Brain imaging in Alzheimer disease. Cold Spring Harb. Perspect. Med. 2, a006213.
Kantarci, K., Gunter, J.L., Tosakulwong, N., Weigand, S.D., Senjem, M.S., Petersen, R.C., Aisen, P.S., Jagust, W.J., Weiner, M.W., Jack, C.R., 2013. Focal hemosiderin deposits and β-amyloid load in the ADNI cohort. Alzheimers Dement. 9, S116–S123.
Kawai, M., Kalaria, R.N., Cras, P., Siedlak, S.L., Velasco, M.E., Shelton, E.R., Chan, H.W., Greenberg, B.D., Perry, G., 1993. Degeneration of vascular muscle cells in cerebral amyloid angiopathy of Alzheimer disease. Brain Res. 623, 142–146.
Klafki, H.-W., Staufenbiel, M., Kornhuber, J., Wiltfang, J., 2006. Therapeutic approaches to Alzheimer's disease. Brain 129, 2840–2855.
Klohs, J., Rudin, M., Shimshek, D.R., Beckmann, N., 2014. Imaging of cerebrovascular pathology in animal models of Alzheimer's disease. Front. Aging Neurosci. 6, 1–30.
Kuo, Y.M., Beach, T.G., Sue, L.I., Scott, S., Layne, K.J., Kokjohn, T.A., Kalback, W.M., Luehrs, D.C., Vishnivetskaya, T.A., Abramowski, D., Sturchler-Pierrat, C., Staufenbiel, M., Weller, R.O., Roher, A.E., 2001. The evolution of A beta peptide burden in the APP23 transgenic mice: implications for A beta deposition in Alzheimer disease. Mol. Med. 7, 609–618.
Levites, Y., Das, P., Price, R.W., Rochette, M.J., Kostura, L.A., McGowan, E.M., Murphy, M.P., Golde, T.E., 2006. Anti-Abeta42- and anti-Abeta40-specific mAbs attenuate amyloid deposition in an Alzheimer disease mouse model. J. Clin. Invest 116, 193–201.
Luo, F., Rustay, N.R., Ebert, U., Hradil, V.P., Cole, T.B., Llano, D.A., Mudd, S.R., Zhang, Y., Fox, G.B., Day, M., 2012. Characterization of 7- and 19-month-old Tg2576 mice using multimodal in vivo imaging: limitations as a translatable model of Alzheimer's disease. Neurobiol. Aging 33, 933–944.
Meyer-Luehmann, M., Mora, J.R., Mielke, M., Spires-Jones, T.L., de Calignon, A., von Andrian, U.H., Hyman, B.T., 2011. T cell mediated cerebral hemorrhages and microhemorrhages during passive Aβ immunization in APPPS1 transgenic mice. Mol. Neurodegener 6, 22.
Neumann, U., Rueeger, H., Machauer, R., Veenstra, S.J., Lueoend, R.M., Tintelnot-Blomley, M., Laue, G., Beltz, K., Vogg, B., Schmid, P., Frieauff, W., Shimshek, D.R., Staufenbiel, M., Jacobson, L.H., 2015. A novel BACE inhibitor NB-360 shows a superior pharmacological profile and robust reduction of amyloid-β and neuroinflammation in APP transgenic mice. Mol. Neurodegener. 10, 44.
Nicoll, J.A.R., Wilkinson, D., Holmes, C., Steart, P., Markham, H., Weller, R.O., 2003. Neuropathology of human Alzheimer disease after immunization with amyloid-beta peptide: a case report. Nat. Med. 9, 448–452.
Nicoll, J.A.R., Yamada, M., Frackowiak, J., Mazur-Kolecka, B., Weller, R.O., 2004. Cerebral amyloid angiopathy plays a direct role in the pathogenesis of Alzheimer's disease. Pro-CAA position statement. Neurobiol. Aging 25, 589–597 discussion 603–4.
O'Brien, J.T., Erkinjuntti, T., Reisberg, B., Roman, G., Sawada, T., Pantoni, L., Bowler, J.V., Ballard, C., DeCarli, C., Gorelick, P.B., Rockwood, K., Burns, A., Gauthier, S., DeKosky, S.T., 2003. Vascular cognitive impairment. Lancet Neurol. 2, 89–98.
Orgogozo, J.-M., Gilman, S., Dartigues, J.-F., Laurent, B., Puel, M., Kirby, L.C., Jouanny, P., Dubois, B., Eisner, L., Flitman, S., Michel, B.F., Boada, M., Frank, A., Hock, C., 2003. Subacute meningoencephalitis in a subset of patients with AD after Abeta42 immunization. Neurology 61, 46–54.
Paganetti, P.A., Lis, M., Klafki, H.W., Staufenbiel, M., 1996. Amyloid precursor protein truncated at any of the gamma-secretase sites is not cleaved to beta-amyloid. J. Neurosci. Res. 46, 283–293.
Park, J.-H., Seo, S.W., Kim, C., Kim, G.H., Noh, H.J., Kim, S.T., Kwak, K.-C., Yoon, U., Lee, J.M., Lee, J.W., Shin, J.S., Kim, C.H., Noh, Y., Cho, H., Kim, H.J., Yoon, C.W., Oh, S.J., Kim, J.S., Choe, Y.S., Lee, K.-H., Lee, J.-H., Ewers, M., Weiner, M.W., Werring, D.J., Na, D.L., 2013. Pathogenesis of cerebral microbleeds: in vivo imaging of amyloid and subcortical ischemic small vessel disease in 226 individuals with cognitive impairment. Ann. Neurol. 73, 584–593.
Pfeifer, M., Boncristiano, S., Bondolfi, L., Stalder, A., Deller, T., Staufenbiel, M., Mathews, P.M., Jucker, M., 2002. Cerebral hemorrhage after passive anti-Abeta immunotherapy. Science 298, 1379.
Racke, M.M., Boone, L.I., Hepburn, D.L., Parsadainian, M., Bryan, M.T., Ness, D.K., Piroozi, K.S., Jordan, W.H., Brown, D.D., Hoffman, W.P., Holtzman, D.M., Bales, K.R., Gitter, B.D., May, P.C., Paul, S.M., DeMattos, R.B., 2005. Exacerbation of cerebral amyloid angiopathy-associated microhemorrhage in amyloid precursor protein transgenic mice by immunotherapy is dependent on antibody recognition of deposited forms of amyloid beta. J. Neurosci. 25, 629–636.
Roher, A.E., Cribbs, D.H., Kim, R.C., Maarouf, C.L., Whiteside, C.M., Kokjohn, T.A., Daugs, I.D., Head, E., Liebsack, C., Serrano, G., Belden, C., Sabbagh, M.N., Beach, T.G., 2013. Bapineuzumab alters aβ composition: implications for the amyloid cascade hypothesis and anti-amyloid immunotherapy. PLoS One 8, e59735.
Sakai, K., Boche, D., Carare, R., Johnston, D., Holmes, C., Love, S., Nicoll, J.A.R., 2014. Aβ immunotherapy for Alzheimer's disease: effects on apoE and cerebral vasculopathy. Acta Neuropathol. 128, 777–789.
Salloway, S., Sperling, R., Gilman, S., Fox, N.C., Blennow, K., Raskind, M., Sabbagh, M., Honig, L.S., Doody, R., van Dyck, C.H., Mulnard, R., Barakos, J., Gregg, K.M., Liu, E., Lieberburg, I., Schenk, D., Black, R., Grundman, M., 2009. A phase 2 multiple ascending dose trial of bapineuzumab in mild to moderate Alzheimer disease. Neurology 73, 2061–2070.
Sperling, R.A., Jack, C.R., Black, S.E., Frosch, M.P., Greenberg, S.M., Hyman, B.T., Scheltens, P., Carrillo, M.C., Thies, W., Bednar, M.M., Black, R.S., Brashear, H.R., Grundman, M., Siemers, E.R., Feldman, H.H., Schindler, R.J., 2011. Amyloid-related imaging abnormalities in amyloid-modifying therapeutic trials: recommendations from the Alzheimer's Association Research Roundtable Workgroup. Alzheimers Dement. 7, 367–385.
Sturchler-Pierrat, C., Abramowski, D., Duke, M., Wiederhold, K.H., Mistl, C., Rothacher, S., Ledermann, B., Bürki, K., Frey, P., Paganetti, P.A., Waridel, C., Calhoun, M.E., Jucker, M., Probst, A., Staufenbiel, M., Sommer, B., Istl, C.L.M., Othacher, S.A.R., Edermann, B.I.L., Urt, K.B.U., 1997. Two amyloid precursor protein transgenic mouse models with Alzheimer disease-like pathology. Proc. Natl. Acad. Sci. U. S. A. 94, 13287–13292.
Sturchler-Pierrat, C., Staufenbiel, M., 2000. Pathogenic mechanisms of Alzheimer's disease analyzed in the APP23 transgenic mouse model. Ann. N. Y. Acad. Sci. 920, 134–139.
Thal, D.R., Griffin, W.S.T., de Vos, R.A.I., Ghebremedhin, E., 2008. Cerebral amyloid angiopathy and its relationship to Alzheimer's disease. Acta Neuropathol. 115, 599–609.
van der Flier, W.M., 2012. Clinical aspects of microbleeds in Alzheimer's disease. J. Neurol. Sci. 322, 56–58.
Vinters, H.V., 1987. Cerebral amyloid angiopathy. A critical review. Stroke 18, 311–324.
Viswanathan, A., Greenberg, S.M., 2011. Cerebral amyloid angiopathy in the elderly. Ann. Neurol. 70, 871–880.
Wilcock, D.M., Rojiani, A., Rosenthal, A., Subbarao, S., Freeman, M.J., Gordon, M.N., Morgan, D., 2004. Passive immunotherapy against Abeta in aged APP-transgenic mice reverses cognitive deficits and depletes parenchymal amyloid deposits in spite of increased vascular amyloid and microhemorrhage. J. Neuroinflammation 1, 24.
Winkler, D.T., Bondolfi, L., Herzig, M.C., Jann, L., Calhoun, M.E., Wiederhold, K.H., Tolnay, M., Staufenbiel, M., Jucker, M., 2001. Spontaneous hemorrhagic stroke in a mouse model of cerebral amyloid angiopathy. J. Neurosci. 21, 1619–1627.
Yamada, M., 2000. Cerebral amyloid angiopathy: an overview. Neuropathology 20, 8–22.
Yates, P.A., Desmond, P.M., Phal, P.M., Steward, C., Szoeke, C., Salvado, O., Ellis, K.A., Martins, R.N., Masters, C.L., Ames, D., Villemagne, V.L., Rowe, C.C., 2014. Incidence of cerebral microbleeds in preclinical Alzheimer disease. Neurology 82, 1266–1273.
Yates, P.A., Sirisriro, R., Villemagne, V.L., Farquharson, S., Masters, C.L., Rowe, C.C., 2011. Cerebral microhemorrhage and brain β-amyloid in aging and Alzheimer disease. Neurology 77, 48–54.
Zago, W., Schroeter, S., Guido, T., Khan, K., Seubert, P., Yednock, T., Schenk, D., Gregg, K.M., Games, D., Bard, F., Kinney, G.G., 2013. Vascular alterations in PDAPP mice after anti-Aβ immunotherapy: implications for amyloid-related imaging abnormalities. Alzheimers Dement. 9, S105–S115.
Zhang-Nunes, S.X., Maat-Schieman, M.L.C., van Duinen, S.G., Roos, R.A.C., Frosch, M.P., Greenberg, S.M., 2006. The cerebral beta-amyloid angiopathies: hereditary and sporadic. Brain Pathol. 16, 30–39.